

# The upper-level circulation anomaly over Central Asia and its relationship to the Asian monsoon and mid-latitude wave train in early summer

Takeshi Watanabe · Koji Yamazaki

Received: 27 December 2012 / Accepted: 16 July 2013  
© Springer-Verlag Berlin Heidelberg 2013

**Abstract** A large intraseasonal variation in geopotential height over the Central Asia region, where the Asian subtropical jet is located, occurs between May and June, and the most dominant variation has a wave-like distribution. This variation in geopotential height influences precipitation across South and Southeast Asia. In this paper, we use composite analysis to determine the causes of this intraseasonal variation over Central Asia. The wave train propagates from the northern Atlantic Ocean to Central Asia over a period of a week, and generates an anomaly in geopotential height over the region. The tropical disturbance, which is similar to the Madden–Julian oscillation, appears a few days before the maximum of the anticyclonic anomaly over Central Asia, and is accompanied by active convection over the Indian Ocean and suppressed convection over Central America. Results of numerical experiments using a linear baroclinic model show that the active convection over the northern Indian Ocean causes the anticyclonic anomaly over Central Asia. The wave train that extends from the northern Atlantic Ocean to Central

Asia is generated by negative thermal forcing over Central America, and the phase distribution of this wave train is similar to that observed in the composite analysis. Central Asia is the region where the effects of the tropics and middle latitudes overlap, and it is an important connection point between the Asian monsoon and middle latitudes.

**Keywords** Asian summer monsoon · Intraseasonal variability · Mid-latitude wave train · Madden–Julian oscillation

## 1 Introduction

The Asian summer monsoon shows distinct intraseasonal variability, which often causes remarkable variations in weather conditions such as precipitation and temperature. This intraseasonal variation is influenced by disturbances both in the tropics and at higher latitudes; i.e., the middle latitudes and the subtropics. The Madden–Julian oscillation (MJO) is one of the most important sources of the intraseasonal variation from the tropics (Madden and Julian 1994; Kemball-Cook and Wang 2001; Pai et al. 2011). As the active convective part of the MJO arrives in the Indian Ocean and moves eastwards into the maritime continent, precipitation in South and Southeast Asia tends to increase (Pai et al. 2011). Kemball-Cook and Wang (2001) investigated boreal summer intraseasonal variation during two separate periods (May–June and August–October) because of the pronounced differences in their climatologies. During both periods, convection over the Indian Ocean propagates along the equator and then moves poleward. This poleward shift of convection is related to Rossby waves emitted by the equatorial convection. Convection in May–June shows strong eastward propagation *along* the equator in both the Indian and western

---

T. Watanabe (✉)  
Graduate School of Environmental Science, Hokkaido University, Kita 10, Nishi 5, Kita-ku, Sapporo, Hokkaido 060-0810, Japan  
e-mail: nabetake@ees.hokudai.ac.jp

T. Watanabe  
Research and Information Center, Tokai University, Tokyo, Japan

K. Yamazaki  
Faculty of Environmental Earth Science, Hokkaido University, Sapporo, Japan

K. Yamazaki  
National Institute of Polar Research, Tachikawa, Japan

Pacific Oceans the maritime continent, while convection in August–October has a weaker eastward-propagating signal along the equator and shows a discontinuous jump from the Indian Ocean to the western Pacific.

Previous studies have shown the relationship between the Asian monsoon and anomalies in the middle latitudes and subtropics, and have indicated that the wave train at higher latitudes is connected to variation in the Asian summer monsoon (Fujinami and Yasunari 2004; Ding and Wang 2007; Krishnan et al. 2009; Watanabe and Yamazaki 2012). These studies also found a marked anomaly over Central Asia and the western Tibetan Plateau. Ding and Wang (2007) showed that a Rossby wave train across the Eurasian continent, and the summer monsoon convection in northwestern India and Pakistan, are coupled at an intraseasonal timescale, and hypothesized a positive feedback between the Eurasian wave train and the South summer monsoon. Watanabe and Yamazaki (2012) showed that the marked anticyclonic geopotential anomaly over the western Tibetan Plateau generates the low-level Rossby wave along the strong westerly duct from the Arabian Sea to Southeast Asia in early summer. Subsequently, the circulation at lower levels changes in South and Southeast Asia. As shown in detail in Sect. 4, the intraseasonal variation in geopotential height over Central Asia and the western Tibetan Plateau is large in the early summer (Fig. 1). The above studies emphasize the influence of the middle latitudes on the tropical monsoon. However, tropical convection also affects the mid-latitude atmospheric circulation. For instance, convection in the South and Southeast Asian monsoons influences the vertical motion over southwestern and Central Asia in the subtropics (Rodwell and Hoskins 1996; Zhang et al. 2004). This suggests that the anomaly extending from Central Asia to the western Tibetan Plateau is an important connection point in the relationship between the subtropics and the Asian summer monsoon.

The basic condition of the atmosphere over Asia changes considerably as the seasons change during the summer monsoon season. The Asian subtropical jet migrates northwards between May and June, and is located around 40°N

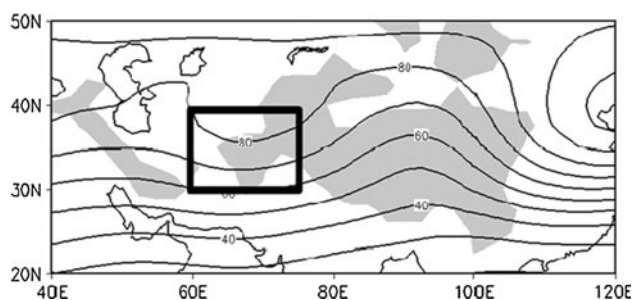


**Fig. 1** Root-mean-square of the modified anomaly of the geopotential height at 200 hPa from May to June for the 45 years from 1958 to 2002. Contour interval is 10 m. The *rectangle* represents the region where the GHP index is defined

between July and August (Schiemann et al. 2009). The low-level westerly that blows from South to Southeast Asia begins to strengthen in May (Webster et al. 1998). At the onset of the Asian summer monsoon, this westerly accelerates rapidly, and then dominates the South and Southeast Asian monsoon regions until October. Tamura et al. (2010) observed an abrupt temperature increase over the Tibetan Plateau during the onset phase of the Asian summer monsoon and showed that the step-wise increase in temperature is caused not only by diabatic heating from the surface of the Tibetan Plateau, but also adiabatic subsidence in the upper level. These abrupt changes in the atmospheric condition cause a distinct change in precipitation throughout the Asian monsoon region (Ueda and Yasunari 1998; Fujinami and Yasunari 2001).

To investigate the intraseasonal variability in the Asian summer monsoon, it is preferable to divide the summer monsoon season into distinct periods, as shown by Kemball-Cook and Wang (2001). Early summer, between May and June, represents the transition season for the Asian summer monsoon (Zhang and Wang 2008). Kajikawa et al. (2012) reported an advance of the onset of the Asian monsoon between 1979 and 2008, attributed to the heat contrast between the Asian landmass and the tropical Indian Ocean; the heating trend over the Asian landmass is the main contributor to the heat contrast. Their Fig. 4 clearly shows landmass heating over the Iranian Plateau and around the western Tibetan Plateau in the subtropics. The relationship between the Asian summer monsoon and the higher latitudes seems to be important for the intraseasonal variability in the Asian summer monsoon in early summer.

This study aims to develop a better understanding of the relationship between the intraseasonal variations in the Asian summer monsoon and variation at higher latitudes, and focuses on the variation in geopotential height over the western Tibetan Plateau during early summer. The remainder of this manuscript is organized as follows. Sections 2 and 3 describe the data and methods used, respectively. Section 4 defines an index that represents the variation in geopotential height over the western Tibetan Plateau and shows the results of a composite analysis involving this index. Section 5 discusses the mechanism that drives the variation in geopotential height over the western Tibetan Plateau, and Sect. 6 describes the results of the numerical linear baroclinic model experiment. Finally, the results are summarized in Sect. 7.

## 2 Data

Three meteorological datasets were used in this study.

1. The 6-hourly reanalysis data, provided by the European Centre for Medium-Range Weather Forecasts (ECMWF) (ERA40; Uppala et al. 2005) on a

$2.5^\circ \times 2.5^\circ$  grid, were used for May and June between 1958 and 2002. The analyzed variables were zonal and meridional wind velocities, temperature, and geopotential height. Stream function and velocity potential were calculated using the expansion into the spherical harmonics function with a truncation of T25. Daily averaged data were used to remove the influence of diurnal variability.

2. The daily-averaged outgoing longwave radiation (OLR) data, provided by the National Oceanic and Atmospheric Administration/Climatic Diagnosis Centers (NOAA/CDC) on a  $2.5^\circ \times 2.5^\circ$  grid, were available over the period from 1975 to 2002 (Liebmann and Smith 1996).
3. Daily precipitation data on a  $0.5^\circ \times 0.5^\circ$  grid, developed by the Asian Precipitation Highly Resolved Observational Data Integration Towards Evaluation of Water Resources (APHRODITE) project (Yatagai et al. 2009), were available for monsoon Asia ( $60^\circ$ – $150^\circ$ E,  $0^\circ$ – $55^\circ$ N) between 1961 and 2002. The APHRODITE precipitation product is based on rain-gauge observations.

The daily climatology was calculated by averaging the data for each day over the period of each dataset, and then smoothing these data using a 5-day running mean. Anomalies were defined as the deviations from this daily climatology. The anomalies do not include the seasonal cycle, but do include interannual variability.

### 3 Methods

We used a time-lagged composite analysis technique based on two indices defined in this study. One index represents the variation in geopotential height over the western Tibetan Plateau, while the second represents the wave train propagating from the northern Atlantic Ocean to the western Tibetan Plateau. Sets of key days for the two indices were determined using suitable criteria, and detailed descriptions of the two indices are given in Sects. 4 and 5. Time-lagged composites were calculated from selected key days. The composite for a set of key days is represented as *day 0*, while *day  $\pm X$*  represents a lagged-composite for the set of days that are *X* days before/after key days. To remove the effect of the seasonal cycle, an anomaly from the daily climatology was composited.

The two-sided Wilcoxon–Mann–Whitney rank sum test was used as the significance test for the precipitation and OLR data because the distributions of precipitation and OLR are non-Gaussian. The two-sided *t* test was used as the significance test for the temperature, geopotential height, stream function, and velocity potential data. For

horizontal wind, zonal and meridional winds are generally tested separately. In this study, the coordinate system was rotated to align the x-axis parallel to the direction that connects the means of the positive and negative samples. The two-sided *t* test was applied to the new x-component data, and this provided a higher level of statistical significance than the test for the original zonal and meridional winds.

We used a dry linear baroclinic model (LBM), which was constructed based on a linearized AGCM (atmospheric general circulation model) developed at the Center for Climate System Research (CCSR), University of Tokyo, Japan, and the National Institute for Environmental Studies (NIES), Japan (Watanabe and Kimoto 2000). The selected horizontal and vertical resolutions were T21 and 11 levels, respectively. The damping timescale was set at 1 day for the lowest and topmost levels, and 30 days for the other levels.

## 4 Results

### 4.1 Variation in geopotential height at 200 hPa in May and June

Figure 1 shows the root-mean-square of the modified anomaly of the geopotential height at 200 hPa from May to June over the 45 years between 1958 and 2002. A modified time series was obtained by removing the seasonal average of the anomaly of geopotential height in May–June in a year from the original time series. Note that the root-mean-square in Fig. 1 does not include the seasonal cycle and the interannual variation but does include the intraseasonal and synoptic-scale variations. A large variation in geopotential height is seen over the western Tibetan Plateau, Afghanistan, Tajikistan, and other Central Asian countries (herein referred to as the Central Asia region) in May and June, at which time the Asian subtropical jet is located around  $35^\circ$ N. The disturbance induced over the Central Asia region is able to propagate eastwards, along the subtropical jet, which acts as the Rossby waveguide (Ambrizzi and Hoskins 1995).

Figure 2 shows the first eigenvector for the above-mentioned root-mean-square of the modified anomaly of geopotential height at 200 hPa over the Central Asia region and surrounding areas. The eigenvector was obtained from the principal component analysis by applying the generalized spatial weighting matrix that was introduced by Baldwin et al. (2009). The first and second principal components account for 22 and 16 % of total variance, respectively. The first eigenvector has its center of variation over the Central Asia region, and a wave-like distribution along the subtropical jet. The first eigenvector

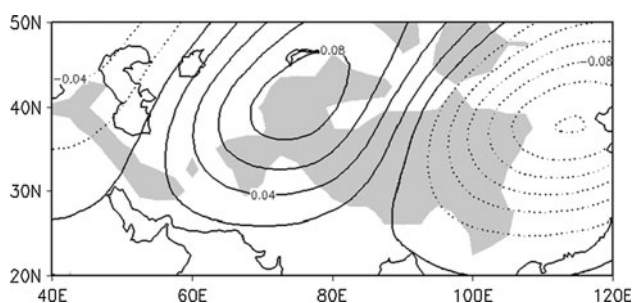


**Fig. 2** First eigenvector for the root-mean-square of the time series of the modified anomaly of geopotential height at 200 hPa shown in Fig. 1. The eigenvector is non-dimensional

calculated from a 5-day low-pass filtered data shows a similar wave-like distribution (figure not shown), which indicates that short-term variations are not dominant in May–June. Consequently, we defined the geopotential height index (the GPH index) as the average anomaly over the Central Asia region ( $30^{\circ}$ – $40^{\circ}$ N,  $60^{\circ}$ – $75^{\circ}$ E; rectangle in Fig. 1), and normalized the index using its standard deviation, as in Watanabe and Yamazaki (2012). For example the time series of the normalized GPH index in 1995 is shown in Fig. 3b. The lagged auto-correlation of the GPH index becomes zero at around a lag of 6 days, which indicates that the upper-level geopotential height anomaly over the Central Asia region shows periodicity at the

monthly scale. The time series in 1995 also shows the monthly-scale periodicity (Fig. 3b).

Composites based on the GPH index were calculated to investigate the relationship between variations in the upper-level geopotential height anomaly over the Central Asia region, and variation in the Asian monsoon in early summer. Two sets of key days, which are positive and negative key days, were determined according to the two criteria that the GPH index is more/less than  $+1.5/-1.5$ . The interval between each key day was set to more than 20 days. This interval is related to the periodicity of the GPH index. If there were several key days within a 20-day period, the largest one was chosen. The composite for positive/negative key days is referred to as the positive/negative composite, respectively, and 35 positive and 40 negative key days were selected over the period of 45 years (Tables 1 and 2).

#### 4.2 Composite analysis based on the GPH index

We now consider the results of the composite analysis based on the GPH index. To emphasize variations related to the upper-level geopotential height over the Central Asia region, the difference between positive and negative composites at the same lag-day (i.e., the composite difference) is shown.

**Fig. 3 a** Time series of area-averaged geopotential height over the Central Asia region in 1995 (thin black line). The thick gray line represents the climatology smoothed with a 5-day running mean. Units are m. **b** Time series of the normalized GPH index in 1995. 13 May is selected as a positive key day, while 25 May and 22 June are selected as negative key days. Arrows denote selected key days

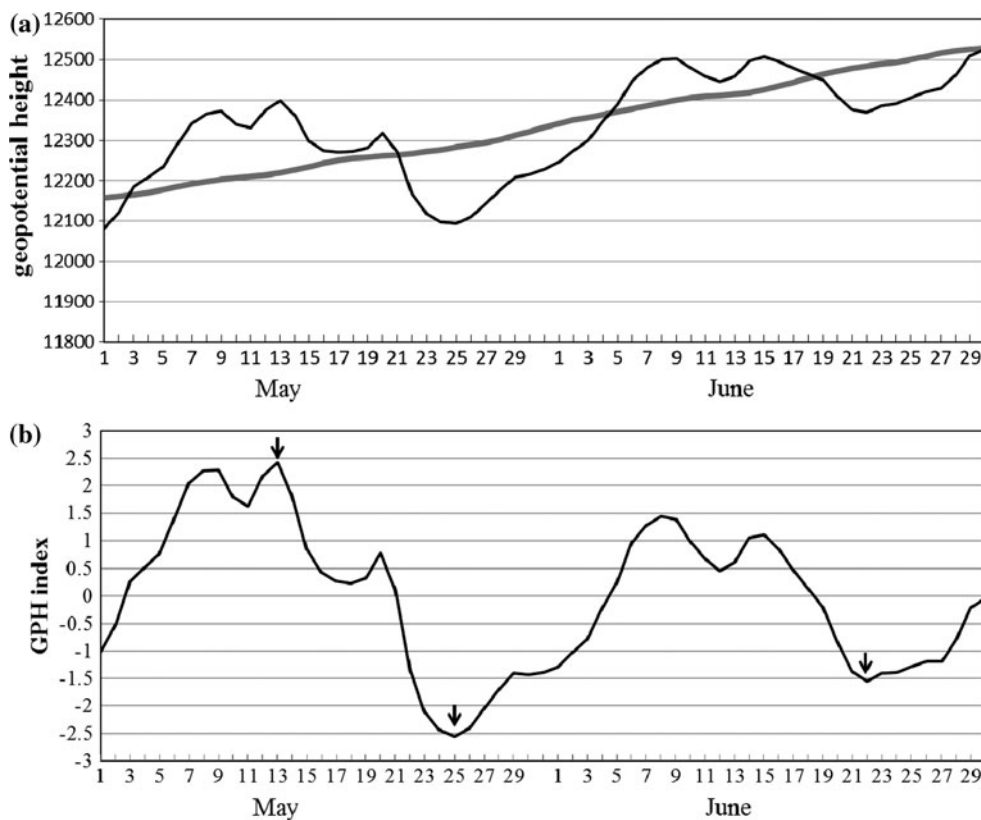


**Table 1** List of key days for the positive composite

3	June	1959	1	May	1959	17	May	1960	3	June	1961	9	May	1961
2	June	1963	16	June	1966	5	May	1966	9	June	1967	28	May	1969
18	May	1970	26	June	1970	9	June	1971	13	June	1973	17	June	1975
6	June	1978	22	June	1980	2	May	1981	7	June	1982	14	June	1984
5	May	1986	6	June	1987	14	May	1990	22	June	1990	15	June	1991
10	June	1993	20	June	1994	13	May	1995	22	June	1996	16	May	1998
28	June	1998	9	May	1999	8	May	2000	12	May	2001	11	May	2002

**Table 2** List of key days for the negative composite

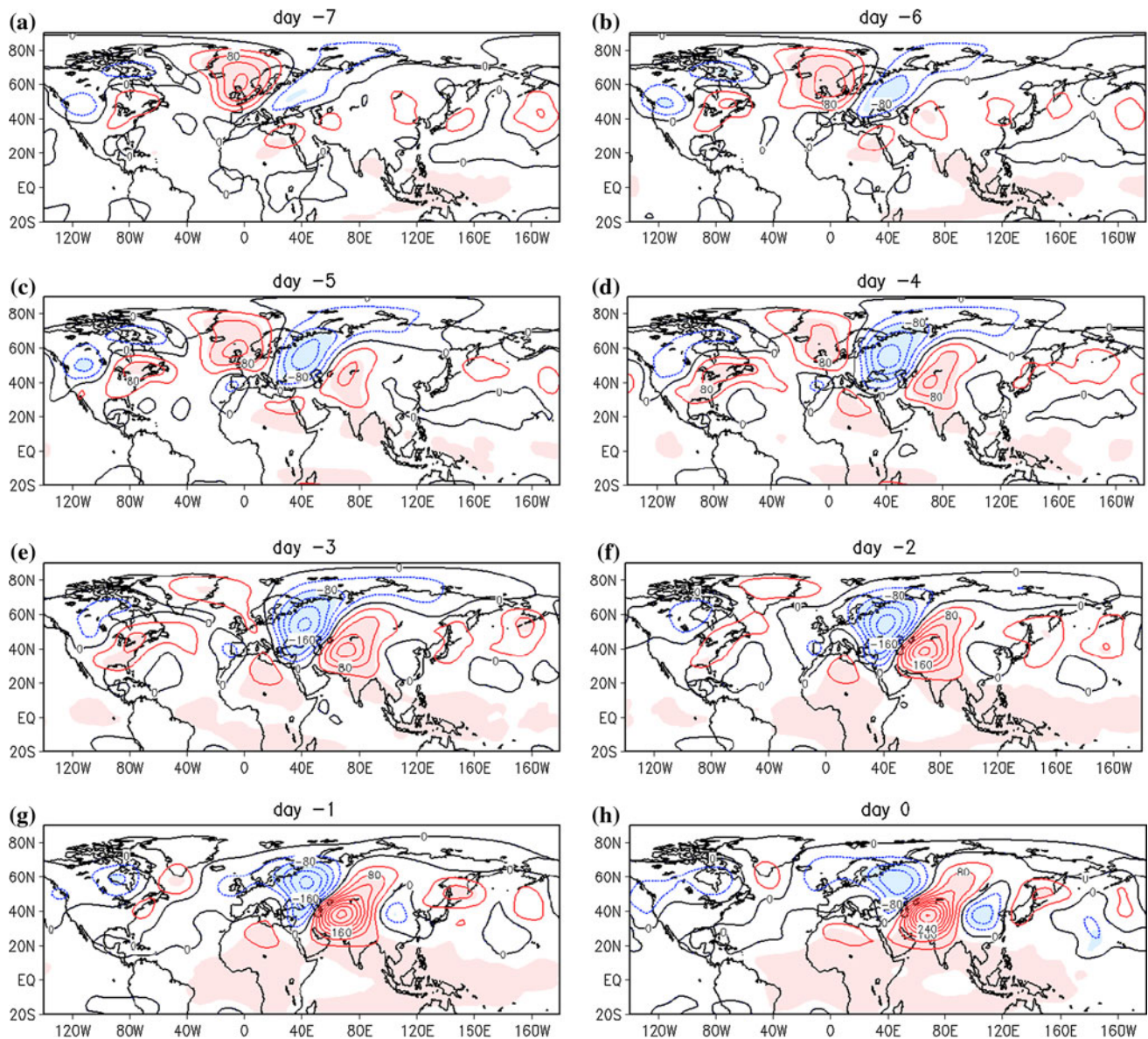
29	May	1958	5	May	1960	29	June	1962	30	June	1963	7	June	1964
11	May	1966	24	May	1967	14	June	1967	7	May	1968	13	May	1969
22	June	1969	6	June	1972	24	June	1974	4	May	1975	9	June	1975
19	June	1976	31	May	1979	14	June	1981	30	June	1982	14	May	1982
14	May	1985	4	June	1986	21	June	1987	7	May	1987	5	June	1988
2	May	1989	21	June	1989	25	June	1991	28	May	1991	4	May	1992
29	May	1992	10	May	1993	25	June	1993	25	May	1995	22	June	1995
14	May	1996	17	May	1997	11	June	1997	14	June	1998	24	June	1999

Figure 4 shows the composite difference of geopotential height at 200 hPa. The wave train propagates from the northern Atlantic Ocean to the Central Asia region via western Russia from day -7 to day 0. Each center of geopotential height anomaly along the propagation path attains a maximum at day -7 over the northern Atlantic Ocean (Fig. 4a), at day -2 over western Russia (Fig. 4f), and at day 0 over the Central Asia region (Fig. 4h). After day 0, the wave train propagates eastwards from the Central Asia region along the subtropical jet.

Figure 5 shows the composite difference for OLR averaged over five days. Between day -9 and day -5 (i.e., the first pentad, centered at day -7), negative OLR anomalies occur over the northern Indian Ocean, and South and Southeast Asia (Fig. 5a), while a positive OLR anomaly is seen over Central America. OLR anomalies are also distributed over North America. OLR anomalies with alternate signs are seen along the propagation route of the wave train from the northern Atlantic Ocean to the Central Asia region in the first and second pentads (Fig. 5a, b). The negative OLR anomalies of more than 20 W/m<sup>2</sup> over the northern Indian Ocean move northwards, and extend across the Arabian Sea, the Indian subcontinent, the Bay of Bengal, Southeast Asia, and south China (Fig. 5b). Simultaneously, the positive OLR anomaly over the Central Asia region intensifies. Between day +1 and day +5; i.e., in the third pentad, the negative OLR anomaly persists from the northern Arabian Sea to south China (Fig. 5c), and a positive OLR anomaly appears over the central Indian Ocean.

The composite for precipitation is consistent with that for OLR over most of Asia, and shows a more detailed distribution of anomalies than OLR (Fig. 6). An increase in precipitation appears along the west coast of the Indian subcontinent, and this enhanced precipitation persists there for about two weeks. A marked increase in precipitation is seen along the southern foothills of the Tibetan Plateau from day +1 to day +5 (Fig. 6c). At the same time, an increase in precipitation is seen along the western coast of Southeast Asia and Myanmar, and the negative anomaly around the Yangtze River basin intensifies. Precipitation over South Asia increases about a week before, and after, day 0. Precipitation tends to increase over the southern part of South Asia (south to 20°N) before day 0, while precipitation increases over the northern part of South Asia after day 0. Precipitation over Southeast Asia increases sharply after day 0.

Figure 7 shows the composite difference for temperature at a height of 2 m averaged over five days. The positive and negative temperature anomalies are distributed from the northern Atlantic Ocean to the Central Asia region alternately (Fig. 7a, b). The black body emission can be estimated from the Stefan-Boltzmann law:  $Q = \sigma T^4$ , where  $\sigma$  is Stefan's constant, and T is the temperature of the black body. The estimated black body emission (not shown) calculated from the composite for temperature at a height of 2 m along the propagation route is comparable with the composites for OLR (Fig. 5a, b). The variation in temperature near the surface from the northern Atlantic Ocean to the Central Asia region is due to the weather



**Fig. 4** Difference between positive and negative composites of geopotential height at 200 hPa from (a) day  $-7$  to (h) day 0. Contour interval is 40 m. Shading represents the 95 % confidence level

conditions under the high/low pressure systems. The OLR anomaly along the Rossby wave propagation route seems to mainly reflect the surface temperature anomaly. The positive temperature anomaly from the Iranian plateau to the Central Asia region is seen between day  $-4$  and day  $+5$  (Fig. 7b, c). These regions are arid. The positive temperature anomaly is caused by the upper-level anticyclonic anomaly, and is connected with the intensification of the heat-low at low levels (Watanabe and Yamazaki 2012). The negative temperature anomaly from South Asia to Southeast Asia persists from the second to the third pentads (Fig. 7b, c). At the same time there occurs an increase in precipitation, and a decrease in OLR (Figs. 5b, c, 6b, c). The estimated black body emission over these regions is

not at all consistent with the OLR anomaly. A large negative OLR anomaly indicates well-developed convective cloud with a high cloud top, and the decrease in near-surface temperature is due to the associated precipitation and cloud cover.

Figure 8 shows the composite difference for horizontal wind at 850 hPa. A westerly anomaly from the Arabian Sea to the Bay of Bengal is seen during the first pentad (Fig. 8a). The anomalous westerlies turn northwards over the Bay of Bengal, and a cyclonic anomaly appears over South Asia. This anomalous westerly moves northwards from the first pentad to the second (Fig. 8b). The anomalous westerlies are accompanied by the OLR anomaly over the Indian Ocean (Fig. 5a, b). This is typical of the

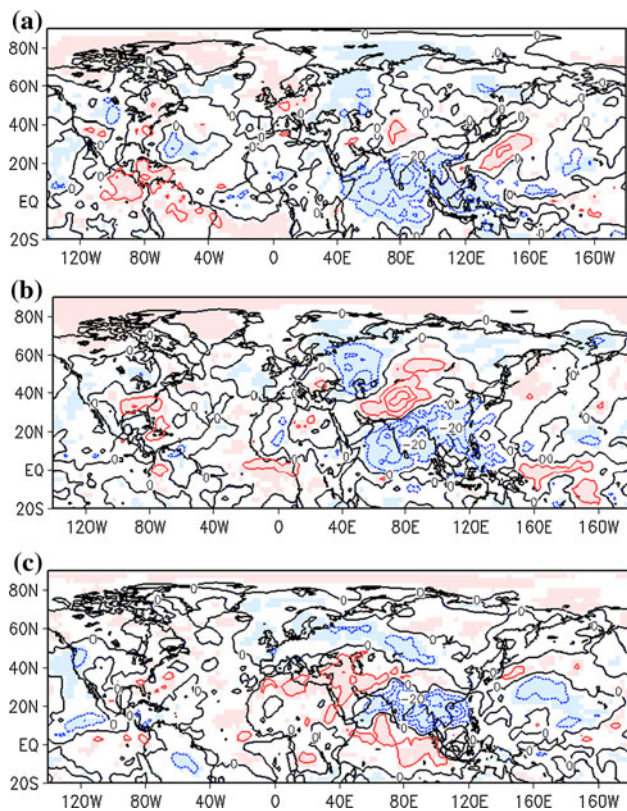


**Fig. 5** Composite difference for OLR averaged between **a** day  $-9$  and day  $-5$ , **b** day  $-4$  and day  $0$ , and **c** day  $+1$  and day  $+5$ . Contours represent OLR. Contour interval is  $10 \text{ W m}^{-2}$ . Shading represents the 95 % confidence level

intraseasonal variation in the summer monsoon season (Yasunari 1979; Kemball-Cook and Wang 2001; Wheeler and Hendon 2004; Wang et al. 2006; Pai et al. 2011). Kemball-Cook and Wang (2001) suggested that the northward migrating disturbance is the Rossby wave emitted by equatorial convection over the Indian Ocean associated with the intraseasonal oscillation. The southwesterlies from the Arabian Sea and the Bay of Bengal are intensified, and the anomalous westerly along  $15^\circ\text{N}$  is evident from the Arabian Sea to Southeast Asia during the third pentad (Fig. 8c). Watanabe and Yamazaki (2012) proposed that the anomalous low-level westerly at  $15^\circ\text{N}$  is induced by the heat-low over Pakistan, which is associated with the upper-level anticyclonic anomaly over Central Asia. The upper-level anomaly there comes from the Atlantic as a wave train (see also Fig. 4). We suggest that the variation in circulation from South and Southeast Asia during the third pentad is caused by the coincidence of the intensified westerly related to the wave train from the mid-latitudes, and Rossby waves caused by the intraseasonal variation in the tropics.

At the same time, an anomalous southwesterly and northwesterly blew towards the southern and northern sides of the western Tibetan Plateau, respectively, and the

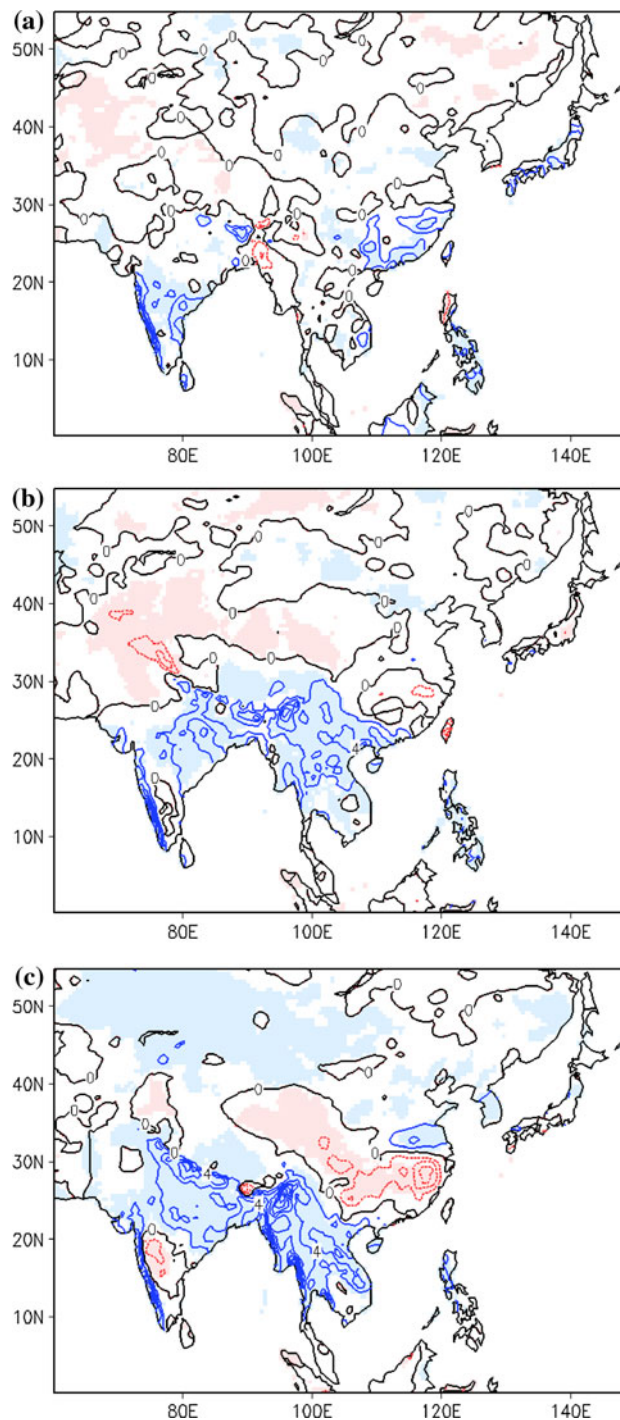


**Fig. 6** As for Fig. 5, but for precipitation. Contour interval is  $2 \text{ mm day}^{-1}$

convergence of these anomalous horizontal winds cause variations in precipitation (Figs. 5c, 6c). The prominent increase in precipitation along the western coast of Southeast Asia and Myanmar is due to the low-level anomalous southwesterly (Fig. 6c). The easterly anomaly over the tropical Pacific Ocean is seen from the first to the

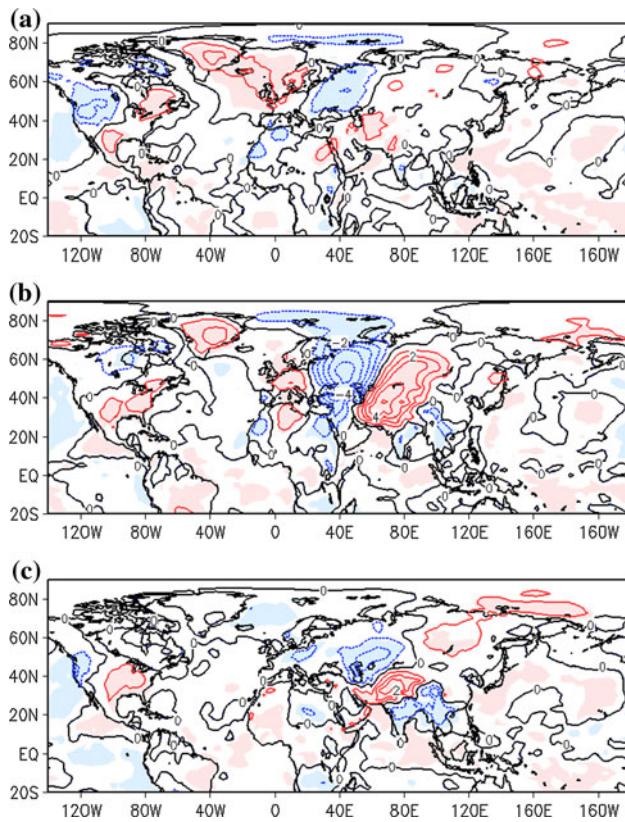


**Fig. 7** As for Fig. 5, but for temperature at a height of 2 m. Contour interval is 1 K

second pentad (Fig. 8a, b). During the third pentad, the easterly anomaly is seen only over the eastern Pacific Ocean (Fig. 8c).

Figure 9 shows the composite difference for the stream function at 200 hPa. Also shown is the wave activity computed from the composite difference for the stream function, based on the climatological basic state in May–June (Takaya and Nakamura 2001). The wave activity flux shows the propagation of the wave train from the northern Atlantic Ocean to the Central Asia region during the first and second pentads, and the eastward propagation along the subtropical jet from the Central Asia region in the third pentad. The scale of the wave activity flux differs between the first pentad and the final two pentads.

Figure 10 shows the composite difference for velocity potential at 200 hPa. The anomalous divergent wind is consistent with the variations in OLR and precipitation (Figs. 5, 6). The disturbance in the tropics, which has the structure of wave number 1, is seen from the first to the last pentad, and migrates eastwards. During the first pentad, an area with active convection is centered on the Indian Ocean, and another area with suppressed convection is centered on Central America (Fig. 10a). The active convection over the northern Indian Ocean causes convergence over the Central Asia region where the developed

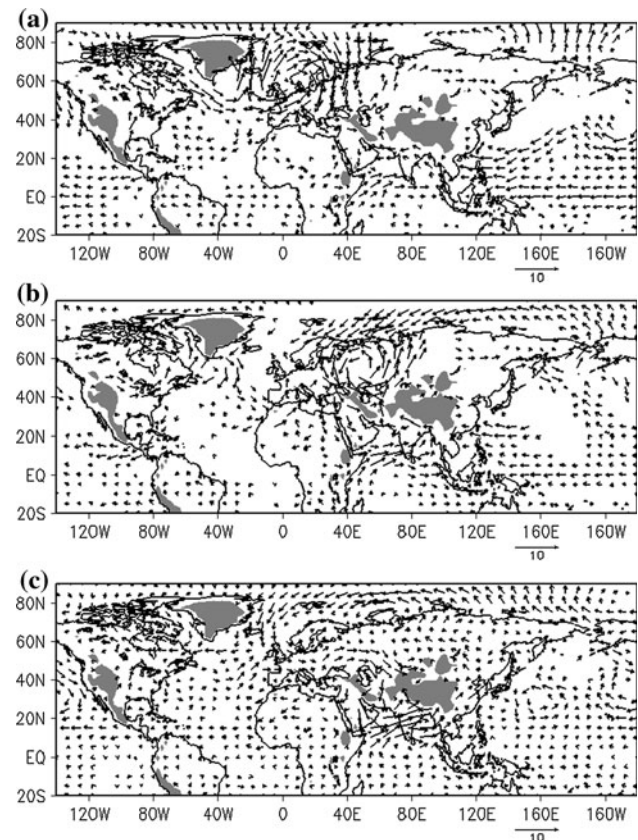


**Fig. 8** As for Fig. 5, but for horizontal wind at 850 hPa. Vector units are  $\text{m s}^{-1}$ . Vectors are only plotted at grid points where the value exceeds the 95 % significance level

anticyclonic anomaly is located (Fig. 10a, b). As shown by Rodwell and Hoskins (1996) and Zhang et al. (2004), the convection over South and Southeast Asia is related to the anomaly over the Central Asia region. We will confirm this relationship using a numerical LBM experiment in Sect. 6. Part of the active convection moves to Southeast Asia and converges to the north between day +1 and day +5, which may cause the decrease in precipitation over the Yangtze River basin (Figs. 6c, 10e).

The results of our composite analysis based on the GHP index show that the variation in the geopotential height anomaly over the Central Asia region is connected to the variation in the early summer Asian monsoon, and is influenced by two factors: propagation of the wave train from the northern Atlantic Ocean to the Central Asia region via western Russia, and convection over the northern Indian Ocean, which is related to disturbance with a wave number of 1 in the tropics. The disturbance in the tropics shows similar characteristics to the MJO. Referring to Wheeler and Hendon (2004) and Pai et al. (2011), composites in this study between day –9 and day –5, and between day –4 and day 0, seem to correspond to phases 3

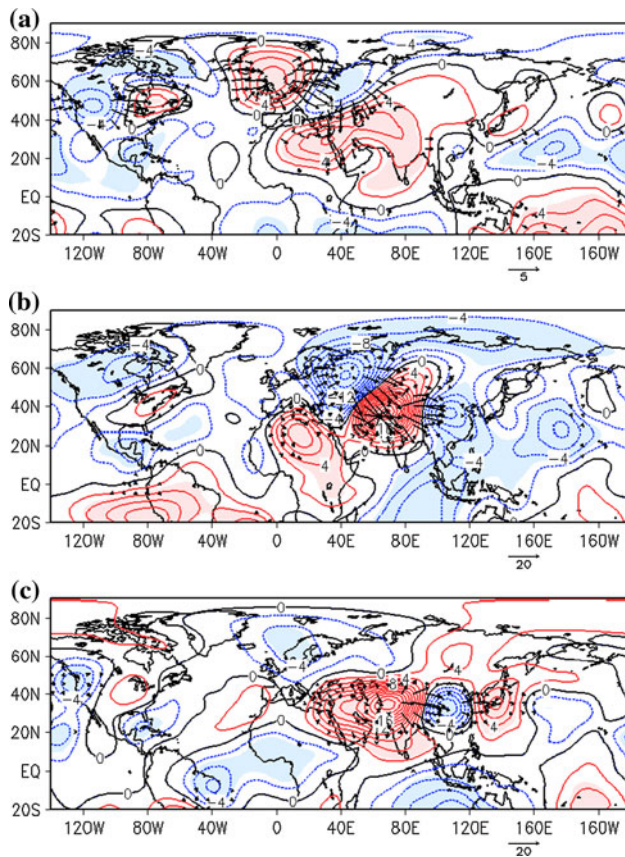


**Fig. 9** As for Fig. 5, but for the stream function at 200 hPa. Contours represent the stream function. Contour interval is  $2 \times 10^6 \text{ m}^2 \text{ s}^{-1}$ . Arrows represent the wave activity flux and are plotted at grid points where the magnitude of wave activity flux is greater than  $1 \text{ m}^2 \text{ s}^{-2}$

and 4 of the MJO index when the active convection is over the Indian Ocean (Wheeler and Hendon 2004). The composite between day +1 and day +5 also resembles phase 5 of the MJO index, except the variation from South Asia to Southeast Asia.

### 5 Wave train propagation to the Central Asia region

In this section, we consider the propagation of the wave train from the northern Atlantic Ocean to the Central Asia region. Firstly, we define an index that represents the propagation of the wave train. We selected three areas where the centers of variation in geopotential height along the propagation route are seen: the northern Atlantic Ocean ( $10^\circ\text{W}$ – $10^\circ\text{E}$ ,  $60^\circ$ – $70^\circ\text{N}$ ), western Russia ( $20^\circ$ – $50^\circ\text{E}$ ,  $50^\circ$ – $60^\circ\text{N}$ ), and the Central Asia region where the GPH index is defined. The average geopotential height anomaly in each area was calculated, and the seasonal change and the interannual variation were removed. Finally, the ARC (Atlantic, Russia, and the Central Asia region) index was

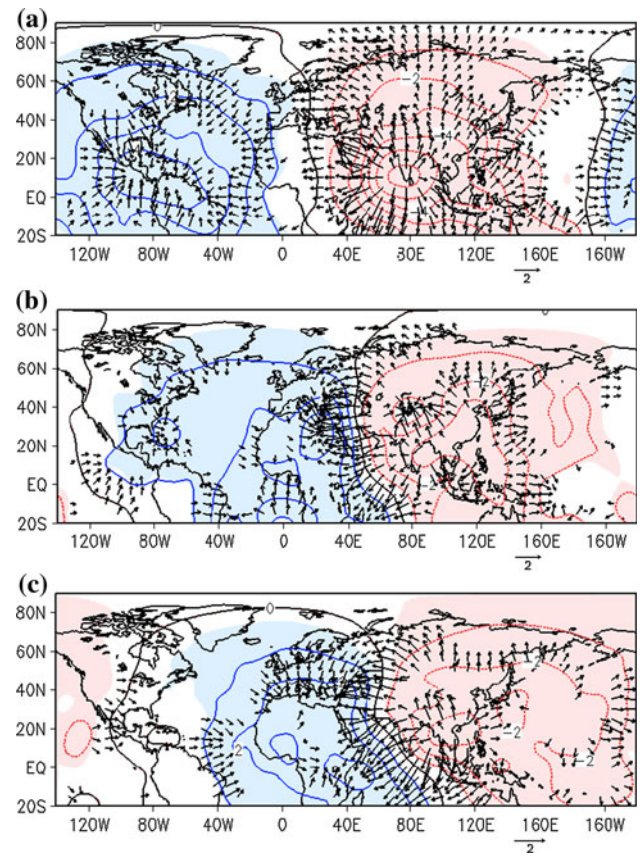


**Fig. 10** As for Fig. 5, but for velocity potential at 200 hPa. Contours represent velocity potential (interval:  $10^5 \text{ m}^2 \text{ s}^{-1}$ ). Arrows represent the divergence wind, and are plotted at grid points where the magnitude of the divergence wind is greater than  $0.5 \text{ m s}^{-1}$

defined as a combination of the three standardized area-averaged geopotential height anomalies:

$$\text{ARC index}(t) = X_A(t - 6) - X_R(t - 2) + X_C(t),$$

where  $X_A$ ,  $X_R$ , and  $X_C$  are the regionally-averaged geopotential height anomalies over the northern Atlantic Ocean, western Russia, and the Central Asia region, respectively, and the number in parentheses denotes the time lag, in days, to the Central Asia region. This lag is determined by the propagation speed (Fig. 4). The term for western Russia is multiplied by  $-1$  because it is opposite in phase to the others. The ARC index excludes interannual variations by removing the seasonal average; consequently, it represents the intraseasonal wave propagation. It is also standardized with its standard deviation. The positive (negative) ARC index represents the propagation from the northern Atlantic Ocean to the Central Asia region via western Russia with a phase distribution of high–low–high (low–high–low). The absolute value of the ARC index reflects the amplitude of the wave train, and its sign shows the phase. The correlation coefficient between the ARC index and the time series of the principal component of the

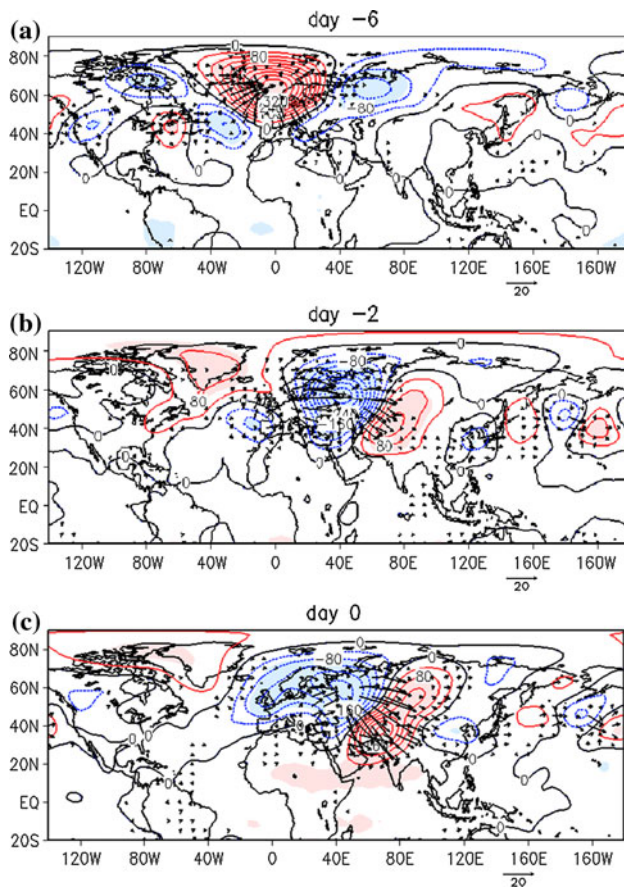


**Fig. 11** Difference between two composites based on the ARC index of geopotential height at 200 hPa at **a** day  $-6$ , **b** day  $-2$ , and **c** day  $0$ . Contour interval is  $40$  m. Arrows represent the wave activity flux and are plotted at grid points where the magnitude of wave activity flux is greater than  $1 \text{ m}^2 \text{ s}^{-2}$

first eigenvector of the variance of geopotential height at 200 hPa over the Central Asia region and surrounding areas (Fig. 2b) is about 0.6 at 95 % confidence level. Although the definition of the ARC index is somewhat subjective, the propagation of the wave train from the northern Atlantic Ocean to the Central Asia region is connected to the dominant variation in geopotential height over the Central Asia region and surrounding areas. Composites involving the ARC index when it was more/less than  $\pm 1.5$  were calculated using the same procedure as for the GPH index.

Figure 11 shows the difference between the positive and negative composites associated with the ARC index for geopotential height at 200 hPa, and the wave activity flux based on the composite difference for stream function. The composite of the ARC index performs well in showing the propagation from the northern Atlantic Ocean to the Central Asia region via western Russia. At day  $-6$ , the high and low anomalies are seen over northeastern North America and to the east (Fig. 10a). The composite of the

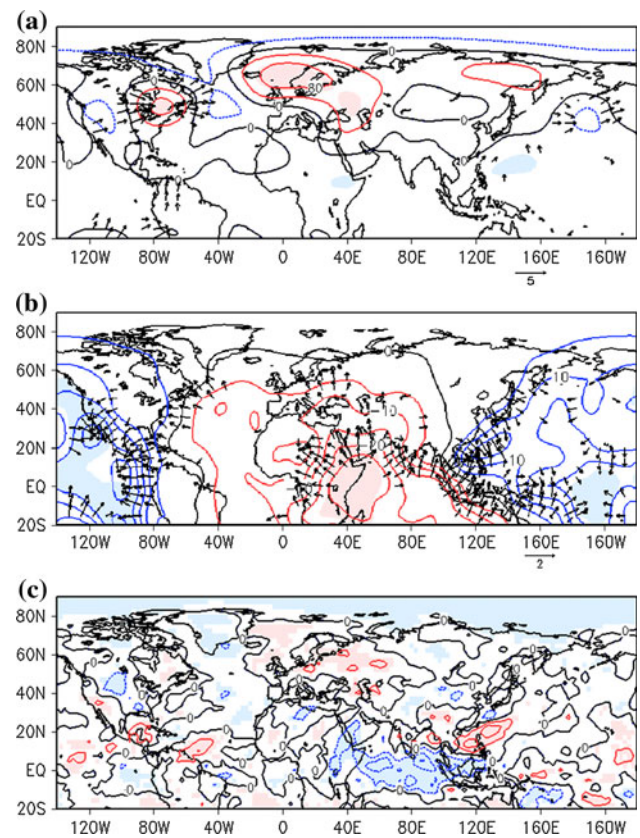


**Fig. 12** As for Fig. 11, but for **a** geopotential height at 200 hPa, **b** velocity potential at 200 hPa, and **c** OLR averaged between day  $-12$  and day  $-8$ . **b** Contour interval is  $5 \times 10^5 \text{ m}^2 \text{ s}^{-1}$ . Arrows represent the divergence wind, and are plotted at grid points where the magnitude of the divergence wind is greater than  $0.5 \text{ m s}^{-1}$ . **c** Contour interval is  $10 \text{ W m}^{-2}$

ARC index is used to trace the propagation of the wave train back, and to seek the source of the wave train.

The composite difference for geopotential height averaged between day  $-12$  and day  $-8$  shows a positive anomaly over the northeast of North America (Fig. 12a). The wave activity flux shows the propagation of the wave train from northeastern North America to the northern Atlantic Ocean. Before day  $-12$  there is no significant signal over North America. The wave train takes about 2 weeks to propagate to the Central Asia region (Fig. 10). After arriving in the Central Asia region, the wave train propagates eastwards along the Asian subtropical jet (not shown).

Figure 12b shows the composite difference for velocity potential at 200 hPa averaged between day  $-12$  and day  $-8$ , and Fig. 12c shows the same composite for OLR. Disturbance with a wave number of 1 is seen in the tropics. The center of active convection is over the Indian Ocean, and the center of suppressed convection is over the central Pacific Ocean, Central America, and the Caribbean Sea. The phase distribution of the disturbance is similar to that

observed in the composite of the GPH index (Fig. 9). We suggest that the marked wave train from northeastern North America to the Central Asia region is related to the MJO-like disturbance.

Barlow and Salstein (2006) and Lorenz and Hartmann (2006) showed that precipitation over Central America is strongly influenced by the MJO. It is most likely that OLR anomalies from the eastern equatorial Pacific Ocean to Central America are related to the MJO-like disturbance. The tropical convection may act as a Rossby-wave source (Sardeshmukh and Hoskins 1988). As indicated by Moon et al. (2013), the convective activity over Mexico and the Caribbean Sea shows a negative correlation with that over South Asia in June–September. They also showed that the teleconnection of convective activity between the North American and South Asian monsoons is due to the quasi-stationary wave train. Their results are similar with those presented here. We suggest that the anomalous divergence/convergence caused by the variation in convection over the eastern Pacific Ocean and Central America is the source of the wave train from northeastern North America to the Central Asia region.

## 6 Numerical LBM experiment

To determine whether the variation in convection over Central America and the northern Indian Ocean, expected from the OLR composites (Figs. 5, 12c), caused the variation in geopotential height over the Central Asia region, two numerical experiments based on the LBM were carried out. As the LBM experiments in this study include only the linear response, we discuss results of the LBM experiments qualitatively, not quantitatively. For simplicity, the same magnitude of heat source was used in both LBM experiments.

In the first experiment, an elliptic heat source with a horizontal  $10^\circ$  radius of  $-8$  K/day was placed over Central America (centered at  $90^\circ\text{W}$ ,  $20^\circ\text{N}$ ) with its maximum at around 500 hPa, and was sustained for the integration period. This thermal forcing mimics the suppressed convection over Central America (Fig. 12c). Atmospheric states were relaxed to the climatology in May–June. Results show the propagation of a wave train from Central America to the Central Asia region (Fig. 13a). The location of each high and low is consistent with composites of the GPH and ARC indexes, and show that variations caused by the tropical disturbance over Central America can contribute to the generation of an ARC wave train with the correct phase. However, anomalies over the northern Atlantic Ocean, western Russia, and the Central Asia region are not large enough to explain the observed values.

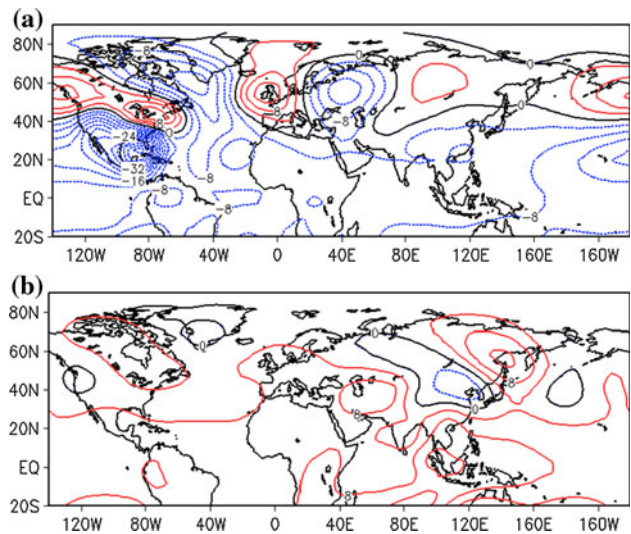


**Fig. 13** Results from **a** the first, and **b** the second numerical LBM experiments showing the 30-day average from day 11 to day 40 of the integration. Contours represent the geopotential height at 200 hPa. Contour interval is 4 m

It seems likely that other dynamical processes, such as transient wave forcing and/or a wave train from another source, reinforces the anomaly over the North Atlantic. We suggest that elaborate models (such as GCMs) will be useful for advanced research into these particulars in a future study.

The second numerical experiment followed the same procedure as the first, except that the thermal forcing was now located over the Indian Ocean ( $90^\circ\text{E}$ ,  $5^\circ\text{N}$ ) to establish the relationship between the geopotential height anomaly over the Central Asia region and the variation in convection over the Indian Ocean in early summer. The results showed an anomalous high over the Central Asia region, and eastward propagation of the wave train (Fig. 13b).

Consequently, the effect of disturbances in the tropics and middle latitudes tends to be concentrated on the Central Asia region. When a large-scale disturbance develops in the tropics, such as the MJO, and the associated active/suppressed convection is located over the Indian Ocean/Central America, a large positive geopotential height anomaly is likely to develop over the Central Asia region.

## 7 Summary

This study investigated the relationship between the geopotential height anomaly over the Central Asia region and variation in the Asian monsoon in the early summer, and has identified one of the mechanisms associated with the variation in the geopotential height anomaly over the Central Asia region. The GPH index is defined as an anomaly of geopotential height over the Central Asia

region, where a large intraseasonal variation in geopotential height is seen. Our approach was based primarily on the composite analysis of this GPH index, and the results are summarized below.

1. The marked geopotential height anomaly over the Central Asia region is related to the wave train in the extratropics. This wave train propagates from the northern Atlantic Ocean via western Russia before arriving at the Central Asia region and generating the geopotential height anomaly there. From the Central Asia region, another wave train propagates eastwards along the Asian subtropical jet.
2. Precipitation and temperature over South and Southeast Asia vary before and after the development of the geopotential anomaly over the Central Asia region. When the considerable positive geopotential anomaly appears over the Central Asia region, precipitation increases over South and Southeast Asia. This variation in precipitation is maintained for about 2 weeks. At the same time, the negative near-surface temperature anomaly extends from South Asia to Southeast Asia. The variation in temperature near the surface from the North Atlantic to the Central Asia region is due to the weather conditions under the high/low pressure systems.
3. A negative OLR anomaly over the northern Indian Ocean precedes the development of the positive geopotential anomaly over the Central Asia region. The composites for velocity potential show an MJO-like disturbance with a wave number of 1 in the tropics. The region where active convection is associated with the disturbance occurs over the Indian Ocean. At the same time, convection is suppressed from the eastern Pacific Ocean to Central America.
4. The wave train that arrives in the Central Asia region can be traced back to northeastern North America 10 days before. A disturbance with a wave number of 1 in the tropics is seen, and is accompanied by positive and negative OLR anomalies over Central America and the Indian Ocean, respectively. The OLR anomaly over Central America is thought to be the source of the wave train from northeastern North America.
5. Two numerical experiments based on the LBM were completed to assess the role of tropical heat sources in the variation in geopotential height over the Central Asia region. In the first experiment, the thermal forcing was located over Central America to generate similar wave train propagation to the composites of the GPH and ARC indexes, although the geopotential height anomaly over the Central Asia region was weak. In the second experiment, the thermal forcing was located over the Indian Ocean, and this also produced a positive

geopotential height anomaly over the Central Asia region. Consequently, tropical heat sources associated with MJO-like disturbances with a wave number of 1 constructively generate the height anomaly over the Central Asia region. The positive (negative) geopotential height anomaly over the Central Asia region develops when convection is active (suppressed) over the Indian Ocean, and is suppressed (active) over the eastern Pacific Ocean and Central America.

**Acknowledgments** The authors thank Prof. F. Hasebe, Dr. M. Inatsu, and Dr. T. Sato for constructive comments on the manuscript, and Prof. M. Watanabe for kindly providing the LBM code. This study was partly supported by the ‘Green Network of Excellence’ Program (GRENE Program) of the Arctic Climate Change Research Project, Japan.

## References

- Ambrizzi T, Hoskins BJ (1995) Rossby wave propagation and teleconnection patterns in the austral winter. *J Atmos Sci* 52:3661–3672
- Baldwin MP, Baldwin MP, Stephenson DB, Jolliffe IT (2009) Spatial weighting and iterative projection methods for EOFs. *J Climate* 22:234–243
- Barlow M, Salstein D (2006) Summertime influence of the Madden-Julian oscillation on daily rainfall over Mexico and Central America. *Geophys Res Lett*. doi:10.1029/2006GL027738
- Ding Q, Wang B (2007) Intraseasonal teleconnection between the summer Eurasian wave train and the Indian monsoon. *J Climate* 20:3751–3767
- Fujinami H, Yasunari T (2001) The seasonal and intraseasonal variability of diurnal cloud activity over the Tibetan Plateau. *J Meteor Soc Jpn* 79:1207–1227
- Fujinami H, Yasunari T (2004) Submonthly variability of convection and circulation over and around the Tibetan Plateau during the boreal summer. *J Meteor Soc Jpn* 82:1545–1564
- Kajikawa Y, Yasunari T, Yoshida S, Fujinami H (2012) Advanced Asian summer monsoon onset in recent decades. *Geophys Res Lett*. doi:10.1029/2011GL050540
- Kemball-Cook S, Wang B (2001) Equatorial waves and air-sea interaction in the boreal summer intraseasonal oscillation. *J Climate* 14:2923–2942
- Krishnan R, Kumar V, Sugi M, Yoshimura J (2009) Internal feedbacks from monsoon-midlatitude interactions during droughts in the Indian summer monsoon. *J Atmos Sci* 66:553–578
- Liebmann B, Smith CA (1996) Description of a complete (interpolated) outgoing longwave radiation dataset. *Bull Am Meteorol Soc* 77:1275–1277
- Lorenz DJ, Hartmann DL (2006) The effect of the MJO on the North America monsoon. *J Climate* 19:333–343
- Madden RA, Julian PR (1994) Observations of the 40-50-day tropical oscillation: a review. *Mon Weather Rev* 122:814–837
- Moon J-Y, Wang B, Ha K-J, Lee J-Y (2013) Teleconnections associated with Northern Hemisphere summer monsoon intraseasonal oscillation. *Clim Dyn* 40:2761–2774. doi:10.1007/s00382-012-1394-0
- Pai DS, Bhat J, Sreejith OP, Hatwar HR (2011) Impact of MJO on the intraseasonal variations of summer monsoon rainfall over India. *Clim Dyn* 36:41–55
- Rodwell MJ, Hoskins BJ (1996) Monsoons and the dynamics of deserts. *Q J R Meteorol Soc* 122:1385–1404

- Sardeshmukh P, Hoskins BJ (1988) The generation of global rotational flow by steady idealized tropical divergence. *J Atmos Sci* 45:1228–1251
- Schiemann R, Luthi D, Schar C (2009) Seasonality and interannual variability of the westerly jet in the Tibetan plateau region. *J Climate* 22:2940–2957
- Takaya K, Nakamura H (2001) A formulation of a phase-independent wave-activity flux for stationary and migratory quasigeostrophic eddies on a zonally varying basic flow. *J Atmos Sci* 58:608–627
- Tamura T, Taniguchi K, Koike T (2010) Mechanism of upper tropospheric warming around the Tibetan Plateau at the onset phase of the Asian summer monsoon. *J Geophys Res.* doi:[10.1029/2008JD01167](https://doi.org/10.1029/2008JD01167)
- Ueda H, Yasunari T (1998) Role of warming over the Tibetan Plateau in early onset of the summer monsoon over the Bay of Bengal and the South China Sea. *J Meteor Soc Jpn* 76:1–12
- Uppala SM et al (2005) The ERA-40 re-analysis. *Q J R Meteorol Soc* 131:2961–3012
- Wang B, Webster PJ, Kikuchi K, Yasunari T, Qi YJ (2006) Boreal summer quasi-monthly oscillation in the global tropics. *Clim Dyn* 27:661–675
- Watanabe M, Kimoto M (2000) Atmosphere-ocean thermal coupling in the north Atlantic: a positive feedback. *Q J R Meteorol Soc* 126:3343–3369
- Watanabe T, Yamazaki K (2012) Influence of the anticyclonic anomaly in the subtropical jet over the western Tibetan Plateau on the intraseasonal variability of the summer Asian monsoon in early summer. *J Climate* 25:1291–1303
- Webster PJ, Magana VO, Palmar TN, Shukla J, Tomas RA, Yanai M, Yasunari T (1998) Monsoon: processes, predictability, and the prospects for prediction. *J Geophys Res* 103:14451–14510
- Wheeler MC, Hendon HH (2004) An all-season real-time multivariate MJO index: development of an index for monitoring and prediction. *Mon Wea Rev* 132:1917–1932
- Yasunari T (1979) Cloudiness fluctuations associated with the northern hemisphere summer monsoon. *J Met Soc Jpn* 57:227–242
- Yatagai A, Arakawa O, Kamiguchi K, Kawamoto H, Nodzu MI, Hamada A (2009) A 44-year daily gridded precipitation dataset for Asia based on a dense network of rain gauges. *SOLA.* doi:[10.2151/sola.2009-035](https://doi.org/10.2151/sola.2009-035)
- Zhang A, Wang B (2008) Global summer monsoon rainy seasons. *Int J Climatol* 28:1563–1578
- Zhang Z, Chan JCL, Ding Y (2004) Characteristics, evolution and mechanisms of the summer monsoon onset over Southeast Asia. *Int J Climatol* 24:1461–1482